

SEMI-ANALYTIC MODELS FOR ELECTRON ACCELERATION IN WEAK ICM SHOCKS

HYESUNG KANG

Department of Earth Sciences, Pusan National University, Busan 46241, Korea; hskang@pusan.ac.kr

Received March 5, 2020; accepted April 14, 2020

Abstract: We propose semi-analytic models for the electron momentum distribution in weak shocks that accounts for both *in situ* acceleration and re-acceleration through diffusive shock acceleration (DSA). In the former case, a small fraction of incoming electrons is assumed to be reflected at the shock ramp and pre-accelerated to the so-called injection momentum, p_{inj} , above which particles can diffuse across the shock transition and participate in the DSA process. This leads to the DSA power-law distribution extending from the smallest momentum of reflected electrons, p_{ref} , all the way to the cutoff momentum, p_{eq} , constrained by radiative cooling. In the latter case, fossil electrons, specified by a power-law spectrum with a cutoff, are assumed to be re-accelerated from p_{ref} up to p_{eq} via DSA. We show that, in the *in situ* acceleration model, the amplitude of radio synchrotron emission depends strongly on the shock Mach number, whereas it varies rather weakly in the re-acceleration model. Considering the rather turbulent nature of shocks in the intracluster medium, such extreme dependence for the *in situ* acceleration might not be compatible with the relatively smooth surface brightness of observed radio relics.

Key words: acceleration of particles — cosmic rays — galaxies: clusters: general — shock waves

1. INTRODUCTION

Cosmological hydrodynamic simulations predicted that the intracluster medium (ICM) on average encounters shocks several times during the formation of the large scale structures in the Universe (e.g., [Ryu et al. 2003](#); [Vazza et al. 2009](#)). As in the case of astrophysical shocks such as the Earth’s bow shock and supernova remnants, ICM shocks are expected to produce cosmic ray protons (CRp) and electrons (CRe) via diffusive shock acceleration (DSA) (e.g. [Bell 1978](#); [Drury 1983](#); [Brunetti & Jones 2014](#)). Many merger-driven shocks have been observed and identified as “radio relic shocks” in the outskirts of galaxy clusters through radio synchrotron radiation from shock-accelerated CRe with Lorentz factor $\gamma_e \sim 10^3 - 10^4$ (e.g. [van Weeren et al. 2010, 2019](#); [Kang et al. 2012](#)). Shocks formed in the hot ICM are weak with sonic Mach numbers $M_s \lesssim 4$, which can be inferred from the observed radio spectral index, $\alpha_\nu = (M_s^2 + 3)/2(M_s^2 - 1)$, using the test-particle prediction of DSA (e.g. [Kang 2011, 2016](#)).

In the following discussion, the shock is specified by the sonic Mach number, M_s , and preshock temperature, T_1 , where the subscripts, 1 and 2, denote the preshock and postshock states, respectively. The momentum distribution, $f(p)$, scales with the upstream gas density, n_1 , and so it does not need to be specified. For quantities related to synchrotron emission and cooling, a preshock magnetic field strength $B_1 = 1 \mu\text{G}$, is adopted. The plasma β refers to the ratio of thermal to magnetic pressures, $\beta = P_{\text{gas}}/P_B$, in the background ICM. Common symbols in physics are used: e.g., m_e for the electron

mass, m_p for the proton mass, c for the speed of light, and k_B for the Boltzmann constant.

Suprathermal particles above the so-called *injection momentum*, p_{inj} , have gyroradii large enough to diffuse across the shock transition and may participate in DSA, a.k.a. Fermi 1st-order acceleration, if scattering MHD/plasma waves of sufficient amplitudes are present (e.g., [Drury 1983](#)). The pre-acceleration of thermal particles to p_{inj} , i.e., the ‘injection problem’, has been a longstanding key problem in the DSA theory (e.g., [Malkov & Drury 2001](#); [Kang et al. 2002](#); [Marcowith et al. 2016](#)). According to plasma simulations of *quasi-parallel* shocks ([Caprioli & Spitkovsky 2014](#); [Caprioli et al. 2015](#); [Ha et al. 2018](#)), some of the incoming protons are specularly reflected by the overshoot in the shock potential and undergo shock drift acceleration (SDA) at the shock front, resulting in the self-excitation of upstream waves via both resonant and non-resonant streaming instabilities. Then the protons are scattered around the shock by those waves, which leads to the formation of the DSA power-law spectrum above $p_{\text{inj}} \sim (3.0 - 3.5)p_{\text{th,p}}$, where $p_{\text{th,p}} = (2m_p k_B T_2)^{1/2}$ is the postshock thermal proton momentum.

On the one hand, electrons are known to be injected and accelerated preferentially at *quasi-perpendicular* shocks, which involves kinetic processes on electron kinetic scales much smaller than ion scales (e.g., [Balogh & Truemann 2013](#)). Earlier studies on the electron pre-acceleration via self-generated waves focused mainly on high Mach number shocks in $\beta \sim 1$ plasma, which are relevant for supernova blast waves (e.g., [Levinson 1992, 1996](#); [Amano & Hoshino 2009](#); [Riquelme & Spitkovsky 2011](#)). [Guo et al. \(2014\)](#) showed, through particle-in-

CORRESPONDING AUTHOR: H. Kang

cell (PIC) simulations, that in weak quasi-perpendicular shocks in high beta ICM plasma, a small fraction of incoming electrons are reflected due to the magnetic mirror and energized via SDA, while the backstreaming electrons excite oblique waves via the electron firehose instability (EFI). Due to scattering of electrons between the shock ramp and EFI-induced waves in the shock foot, the pre-accelerated electrons seem to form a DSA power-law spectrum through a Fermi I-like acceleration. However, Kang et al. (2019) showed that such pre-acceleration is effective only in supercritical shocks with $M_s \gtrsim 2.3$. Moreover, they suggested that suprathermal electrons may not be energized all the way to $p_{\text{inj}} \sim 150p_{\text{th,e}}$ (where $p_{\text{th,e}} = (2m_e k_B T_2)^{1/2}$), because the growth of longer waves via the EFI is saturated. On the other hand, Trotta & Burgess (2019) and Kobzar et al. (2019) have demonstrated through hybrid simulations with test-particle electrons ($\beta \approx 1$) and PIC simulations ($\beta \approx 5$), respectively, that at supercritical quasi-perpendicular shocks the rippling of shock surface excited by Alfvén Ion Cyclotron (AIC) instability could induce multi-scale fluctuations, leading to the pre-acceleration of electrons beyond p_{inj} . Whereas the critical Mach number above which the shock rippling becomes active was estimated to be $M_{\text{A,crit}} \approx 3.5$ for $\beta \approx 1$ shocks (Trotta & Burgess 2019), this problem needs to be investigated for higher β shocks.

Although the DSA model seems to provide a simple and natural explanation for some observed properties of radio relics, such as thin elongated shapes, postshock spectral steepening due to aging electron population, and polarization vectors indicating perpendicular magnetic field directions, there remain some unresolved problems that need further investigation. First of all, the pre-acceleration of thermal electrons to suprathermal energies and the subsequent injection into the DSA process still remains rather uncertain, especially at subcritical shocks with $M_s \lesssim 2.3$ (Kang et al. 2019). Secondly, the fraction of observed merging clusters with detected radio relics is only $\sim 10\%$ (Feretti et al. 2012), while numerous quasi-perpendicular shocks are expected to form in the ICM (Wittor et al. 2017; Roh et al. 2019). Thirdly, in a few cases, the sonic Mach number inferred from X-ray observations is smaller than that estimated from radio spectral index of radio relics, i.e., $M_X < M_{\text{radio}}$ (Akamatsu & Kawahara 2013; Kang 2016). Thus re-acceleration of fossil CRe, pre-existing in the ICM, has been suggested as a possible resolution for these puzzles that the DSA model with ‘*in situ* injection only’ leaves unanswered (e.g., Kang et al. 2012, 2017; Kang 2016).

Based on what we have learned from the previous studies, here we propose semi-analytic models for the momentum distribution function of CRe, $f(p)$, in the two scenarios of DSA at weak quasi-perpendicular shocks in the test-particle regime: (1) an *in situ* acceleration model in which electrons are injected directly from the background thermal pool at the shock, and (2) a re-acceleration model in which pre-existing fossil CRe are accelerated. Although it remains largely unknown if and how CRe are accelerated at subcritical shocks, in

this paper we take a heuristic approach and assume that DSA operates at shocks of all Mach numbers.

In the next section we describe in details the semi-analytic models for $f(p)$ along with an in-depth discussion of the underlying physical justification. In Section 3 we demonstrate how our model can be applied to weak shocks in the ICM and discuss observational implications. A brief summary will be given in Section 4.

2. SEMI-ANALYTIC DSA MODEL

The physics of collisionless shocks depends on various shock parameters including the sonic Mach number, M_s , the plasma β , and the obliquity angle, θ_{Bn} , between the upstream background magnetic field direction and the shock normal (e.g., Balogh & Truemann 2013). For instance, collisionless shocks can be classified as *quasi-parallel* (Q_{\parallel} , hereafter) shocks with $\theta_{\text{Bn}} \lesssim 45^\circ$ and *quasi-perpendicular* (Q_{\perp} , hereafter) shocks with $\theta_{\text{Bn}} \gtrsim 45^\circ$. CRp are known to be accelerated efficiently at Q_{\parallel} -shocks, while CRe are accelerated preferentially at Q_{\perp} -shocks (Gosling et al. 1989; Burgess 2007; Caprioli & Spitkovsky 2014; Guo et al. 2014).

In this study, we focus on the electron acceleration at Q_{\perp} -shocks with $M_s \lesssim 4$ that are expected to form in the ICM. Most of the kinetic problems involved in the electron acceleration, including the shock criticality, excitation of waves via microinstabilities, and wave-particle interactions, have been investigated previously for shocks in $\beta \sim 1$ plasma such as the solar wind and the interstellar medium (see Balogh & Truemann 2013; Marcowith et al. 2016). Although a few studies, using kinetic PIC simulations, have recently considered weak shocks in the high β ICM environment (Guo et al. 2014; Matsukiyo & Matsumoto 2015; Kang et al. 2019; Kobzar et al. 2019), full understanding of the electron injection and acceleration into the regime of genuinely diffusive scattering has yet to come.

The main difficulty in reaching such a goal is the severe computational requirements to perform PIC simulations for high β shocks; the ratio of the proton Larmor radius to the electron skip depth increases with $\beta^{1/2}$. Moreover, to properly study these problems, PIC simulations in at least two-dimensional domains extending up to several proton Larmor radii are required, because kinetic instabilities induced by both protons and electrons may excite waves on multiple scales that propagate in the direction oblique to the background magnetic fields.

2.1. Particle Injection to DSA

In this section, we review the current understanding of the injection problem that has been obtained previously through plasma hybrid and PIC simulations. Suprathermal particles, both protons and electrons, with $p \gtrsim 3p_{\text{th,p}}$ could diffuse across the shock both upstream and downstream, and participate in the DSA process, because the shock thickness is of the order of the gyro-radius of postshock thermal protons. Thus the injection momentum is often parameterized as

$$p_{\text{inj}} = Q_{\text{i,p}} \cdot p_{\text{th,p}}, \quad (1)$$

where the injection parameter is estimated to be in the range $Q_{i,p} \sim 3.0 - 3.5$, according to the hybrid simulations of Q_{\parallel} shocks in $\beta \sim 1$ plasma (Caprioli & Spitkovsky 2014; Caprioli et al. 2015; Ha et al. 2018). On the other hand, Ryu et al. (2019) showed that the DSA power-law with $Q_{i,p} \approx 3.8$ gives a postshock CRp energy density less than 10 % of the shock kinetic energy density for $M_s \lesssim 4$, i.e., $E_{\text{CRp}} < 0.1 E_{\text{sh}}$ (where $E_{\text{sh}} = \rho_1 u_s^2/2$).

The electron injection at Q_{\perp} -shocks involves somewhat different processes, which can be summarized as follows: (1) the reflection of some of the incoming electrons at the shock ramp due to magnetic deflection, leading to a beam of backstreaming electrons, (2) the energy gain from the motional electric field in the upstream region through shock drift acceleration (SDA), (3) the trapping of electrons near the shock due to the scattering by the upstream waves, which are excited by backstreaming electrons via the EFI, and (4) the formation of a suprathermal tail for $p \gtrsim p_{\text{ref}}$ with a power-law spectrum, which seems consistent with the test-particle DSA prediction (Guo et al. 2014; Matsukiyo & Matsumoto 2015). Here, p_{ref} represents the lowest momentum of the reflected electrons above which the suprathermal power-law tail develops. This is again parameterized as

$$p_{\text{ref}} = Q_{i,e} \cdot p_{\text{th},e}, \quad (2)$$

with the injection parameter, which is assumed to be in the range $Q_{i,e} \sim 3.5 - 3.8$ as in the case of p_{inj} (e.g., Guo et al. 2014; Kang et al. 2019).

Recently, Kang et al. (2019) showed that the electron pre-acceleration through the combination of reflection, SDA, and EFI may operate only in *supercritical* Q_{\perp} -shocks with $M_s \gtrsim 2.3$ in $\beta \sim 100$ plasma. In addition, they argued that the EFI alone may not energize the electrons all the way to p_{inj} , unless there are pre-existing turbulent waves with wavelengths longer than those of the EFI-driven waves. As mentioned earlier, on the one hand, Trotta & Burgess (2019) and Kobzar et al. (2019) showed through 2D simulations that the suprathermal tail may extend to beyond p_{inj} in the presence of multi-scale turbulence excited by the shock rippling instability. But Trotta & Burgess (2019) suggested that the critical Mach number, at which the shock surface rippling starts to develop, is $M_s \approx 3.5$ in $\beta \approx 1$ plasma. Hence, we still need to answer the following questions in future studies: (1) if and how the electron injection occurs at subcritical shocks with $M_s \lesssim 2.3$, and (2) how the critical Mach number for the shock surface rippling varies with shock parameters such as β and θ_{Bn} .

On the other hand, X-ray and radio observations of several radio relics indicate the efficient electron acceleration even at subcritical shocks with $1.5 \lesssim M_s \lesssim 2.3$ (van Weeren et al. 2019). Hence, in the discussion below, we heuristically assume that the DSA power-law spectrum of the accelerated electrons, $f_{e,\text{inj}} \propto p^{-q}$ (where $q = 4M_s^2/(M_s^2 - 1)$), develops from $\sim p_{\text{ref}}$ all the way to the cutoff momentum p_{eq} (see below) at Q_{\perp} -shocks of all

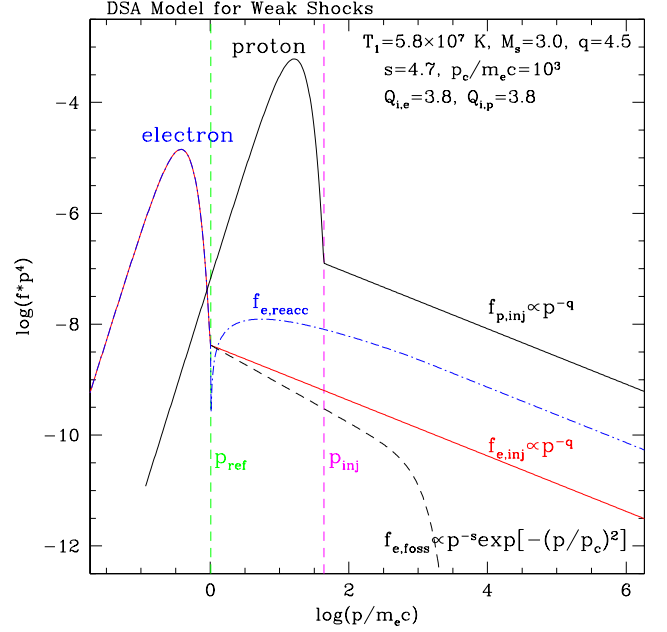


Figure 1. Semi-analytic functions for the momentum distribution, $f(p)p^4$, in a $M_s = 3.0$ shock, based on the test-particle DSA model. The red line shows the injected population, $f_{e,\text{inj}}(p)$, in Equation (6). The black dashed line shows a power-law spectrum of pre-existing fossil electrons, $f_{e,\text{foss}}(p)$, with a slope $s = 4.7$ and a cutoff momentum $p_c/m_e c = 10^3$. The blue dot-dashed line shows the spectrum of re-accelerated electrons, $f_{e,\text{reacc}}(p)$ in Equation (12). The green vertical line denotes $p_{\text{ref}} = Q_{i,e} p_{\text{th},e}$ with $Q_{i,e} = 3.8$, above which suprathermal electrons are reflected at the shock ramp and accelerated by Fermi-I acceleration. Note that the amplitude of $f_{e,\text{reacc}}(p)$ scales with the adopted normalization factor, f_o , and so the relative importance between $f_{e,\text{reacc}}$ and $f_{e,\text{inj}}$ depends on it. The proton spectrum, including both the postshock Maxwellian and injected DSA power-law components, is shown by the black solid line for comparison. The magenta vertical line demarcates the injection momentum, $p_{\text{inj}} = Q_{i,p} p_{\text{th},p}$ with $Q_{i,p} = 3.8$, above which particles can undergo the full DSA process across the shock transition.

Mach numbers. This hypothesis needs to be examined in future studies for high β shocks.

Nevertheless, we refer to Figure 4 of Park et al. (2015), in which the acceleration of both protons and electrons at strong Q_{\parallel} -shocks ($M_s = 40$) were investigated through 1D PIC simulations. There, electrons form a DSA power-law for $p \gtrsim p_{\text{ref}}$, because local fields become quasi-perpendicular at some parts of the shock surface due to turbulent magnetic field amplification driven by the strong non-resonant Bell instability.

2.2. Test-Particle Solutions for the Injection-only Case

Here we adopt the test-particle solutions of DSA, because dynamical feedbacks of CRp and CRe are expected to be insignificant at weak ICM shocks (e.g., Ryu et al. 2019). Then the isotropic part of the momentum distribution function at the shock position can be approximated by a power-law spectrum with a super-

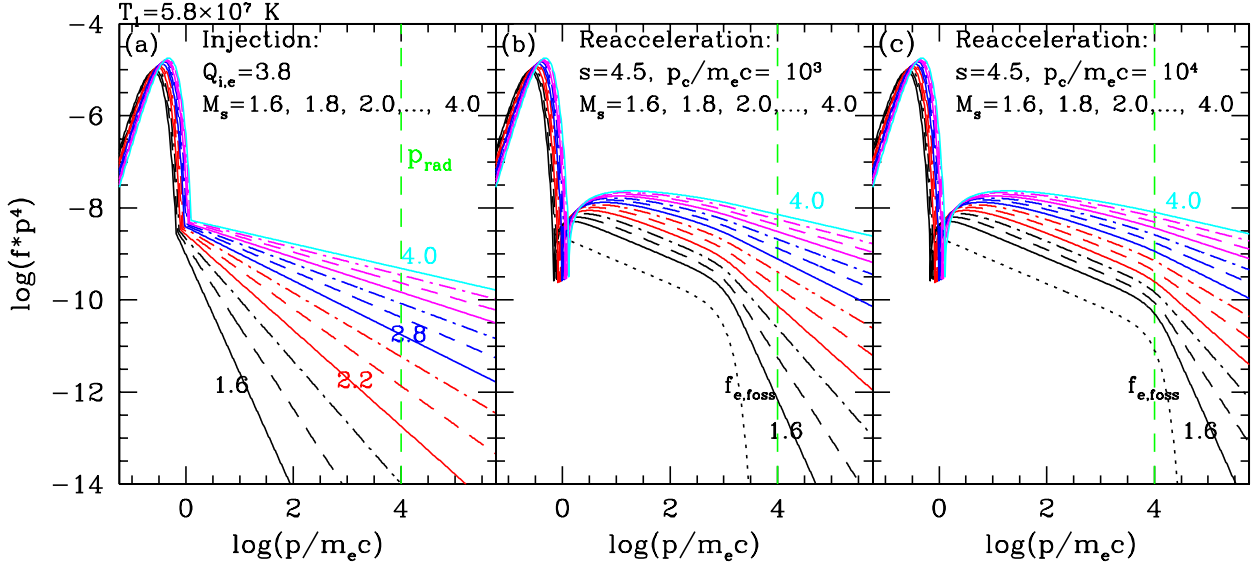


Figure 2. Semi-analytic DSA model for $f(p)p^4$ for shocks with $M_s = 1.6 - 4.0$ and $T_1 = 5.8 \times 10^7$ K: (a) injected spectrum, $f_{e,\text{inj}}(p)$, with $Q_{i,e} = 3.8$, (b) re-accelerated spectrum, $f_{e,\text{reacc}}(p)$, for the power-law spectrum of fossil electrons with $s = 4.5$ and $p_c/m_e c = 10^3$, (c) the same as (b) except $p_c/m_e c = 10^4$. The blue dashed lines correspond to the models with $M_s = 3.0$ and $q = s = 4.5$. Note that the re-accelerated spectrum scales with the normalization factor of $f_{e,\text{foos}}$, i.e., $f_{e,\text{reacc}} \propto f_o$. The green vertical lines denote $p_{\text{rad}}/m_e c = 10^4$.

exponential cutoff. For the CRp spectrum,

$$f_{p,\text{inj}}(p) \approx f_{\text{inj}} \cdot \left(\frac{p}{p_{\text{inj}}}\right)^{-q} \exp\left(-\frac{p^2}{p_{\text{max}}^2}\right). \quad (3)$$

The normalization factor at p_{inj} is given by

$$f_{\text{inj}} = \frac{n_{p,2}}{\pi_{1.5}^{1.5}} p_{\text{th},p}^{-3} \exp(-Q_{i,p}^2), \quad (4)$$

where $n_{p,2}$ is the postshock proton number density. The maximum momentum of CRp at a shock age t can be estimated as

$$\frac{p_{\text{max}}}{m_p c} \approx \frac{\sigma - 1}{6\sigma} \frac{u_s^2}{\kappa^*} t, \quad (5)$$

where $\sigma = n_2/n_1$ is the shock compression ratio and κ^* is the diffusion coefficient at $p = m_p c$ (Kang & Ryu 2011). For ICM shocks, $p_{\text{max}}/m_p c \gg 1$, so the exponential cutoff at p_{max} is not important for weak shocks.

Similarly, the test-particle spectrum of CRe can be expressed as

$$f_{e,\text{inj}}(p) \approx f_{\text{ref}} \cdot \left(\frac{p}{p_{\text{ref}}}\right)^{-q} \exp\left(-\frac{p^2}{p_{\text{eq}}^2}\right). \quad (6)$$

The normalization factor at p_{ref} is given by

$$f_{\text{ref}} = \frac{n_{e,2}}{\pi_{1.5}^{1.5}} p_{\text{th},e}^{-3} \exp(-Q_{i,e}^2), \quad (7)$$

where $n_{e,2}$ is the postshock electron number density. The cutoff momentum, p_{eq} , can be derived from the equilibrium condition that the DSA momentum gains per cycle are equal to the synchrotron/iC losses per cycle

(Kang 2011):

$$p_{\text{eq}} = \frac{m_e^2 c^2 u_s}{\sqrt{4e^3 q/27}} \left(\frac{B_1}{B_{e,1}^2 + B_{e,2}^2}\right)^{1/2}, \quad (8)$$

where the ‘effective’ magnetic field strength $B_e^2 = B^2 + B_{\text{rad}}^2$ takes account for radiative losses due to both synchrotron and iC processes, where $B_{\text{rad}} = 3.24 \mu\text{G}(1+z)^2$ corresponds to the cosmic background radiation at redshift z . Here, we assume the Bohm diffusion for DSA, and set $z = 0.2$ as a reference epoch and so $B_{\text{rad}} = 4.7 \mu\text{G}$. For typical ICM shock parameters, it becomes

$$\frac{p_{\text{eq}}}{m_e c} \approx \frac{6.75 \times 10^9}{q^{1/2}} \left(\frac{u_s}{1000 \text{ km s}^{-1}}\right) \left(\frac{B_1}{B_{e,1}^2 + B_{e,2}^2}\right)^{1/2}, \quad (9)$$

where the magnetic field strength is expressed in units of μG . Again, $p_{\text{eq}}/m_e c \gg 10^4$, so the exponential cutoff is not important for weak shocks.

With the DSA model spectra given in Equations (3) and (6), if $Q_{i,p} = Q_{i,e}$ as assumed here, then the ratio of $f_{p,\text{inj}}$ to $f_{e,\text{inj}}$ at $p = p_{\text{inj}}$ can be estimated as

$$K_{p/e} \equiv \frac{f_{p,\text{inj}}(p_{\text{inj}})}{f_{e,\text{inj}}(p_{\text{inj}})} = \left(\frac{p_{\text{th},p}}{p_{\text{th},e}}\right)^{q-3} = \left(\frac{m_p}{m_e}\right)^{(q-3)/2}, \quad (10)$$

where $K_{p/e}$ is equivalent to the CRp-to-CRe number ratio. For example, in the case of a $M_s = 3.0$ shock with $q = 4.5$, $K_{p/e} = 280$, but with the caveat that protons (electrons) are accelerated at Q_{\parallel} (Q_{\perp}) shocks.

In Figure 1, we illustrate the thermal Maxwellian distribution and the test-particle power-law spectrum,

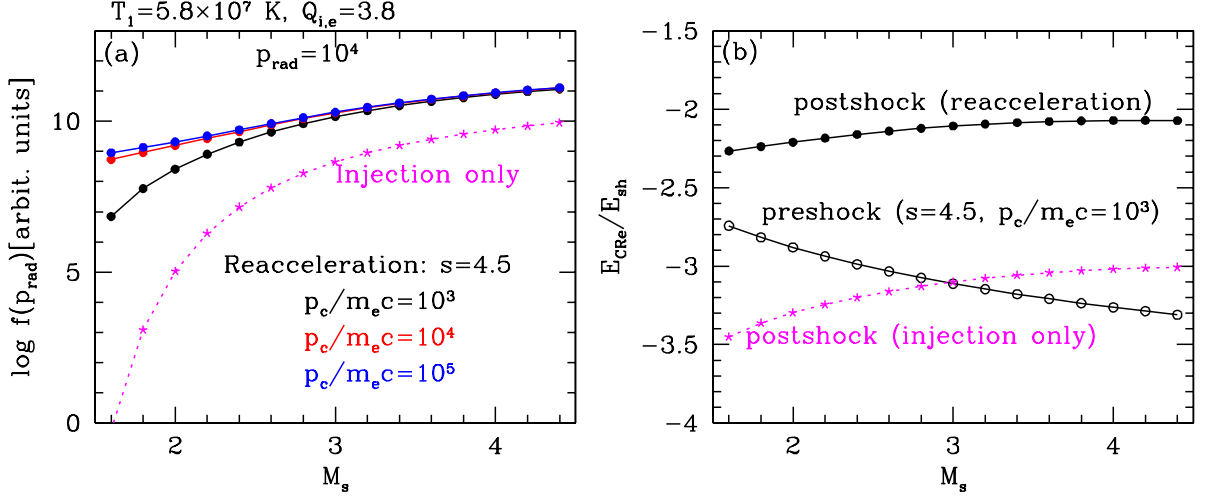


Figure 3. (a) Amplitude of $f(p_{\text{rad}})$ at $p_{\text{rad}} = 10^4 m_e c$ for the re-acceleration case with slope $s = 4.5$ and cutoff momentum $p/m_e c = 10^3$ (black circles), 10^4 (red circles), and 10^5 (blue circles). The magenta line with asterisks shows $f(p_{\text{rad}})$ for the injection-only case. The semi-analytic DSA spectra ($Q_{i,e} = 3.8$) shown in Figure 2 are used. (b) CRe pressure, E_{CRe} , in units of $E_{\text{sh}} = \rho_1 u_s^2/2$. The preshock $E_{\text{CRe},1}$ due to fossil CRe with $s = 4.5$ and $p_c/m_e c = 10^3$ is indicated by open circles, while the postshock $E_{\text{CRe},2}$ due to re-accelerated CRe is indicated by closed circles. The magenta line with asterisks shows $E_{\text{CRe},2}$ for the injection-only case. Again, the semi-analytic DSA spectra in Figure 2 are used.

$f_{p,\text{inj}}(p)$, for protons, which are demarcated by the magenta line of p_{inj} . The shock parameters adopted here are $Q_{i,p} = 3.8$, $M_s = 3$ and $T_1 = 5.8 \times 10^7$ K, and $q = 4.5$. Also, the thermal Maxwellian distribution and $f_{e,\text{inj}}(p)$ for electrons are demarcated by the green line given by p_{ref} with $Q_{i,e} = 3.8$. This clearly demonstrates that, in order to get injected to DSA, the reflected electrons need to be energized by a factor of $p_{\text{inj}}/p_{\text{ref}} \approx \sqrt{m_p/m_e}$.

2.3. Re-acceleration of Fossil CR Electrons

For the preshock population of fossil CRe, we adopt a power-law spectrum with slope s and a cutoff momentum p_c for $p > p_{\text{ref}}$:

$$f_{e,\text{foss}}(p) = f_o \cdot \left(\frac{p}{p_{\text{ref}}}\right)^{-s} \exp\left(-\frac{p^2}{p_c^2}\right), \quad (11)$$

where $p_c/m_e c = 10^3 - 10^5$ is considered in this discussion, and the normalization factor, f_o , determines the amount of fossil CRe. Then, the re-accelerated population at the shock can be calculated semi-analytically by the following integration:

$$f_{e,\text{reacc}}(p) = q \cdot p^{-q} \int_{p_{\text{ref}}}^p p'^{q-1} f_{e,\text{foss}}(p') dp' \quad (12)$$

(Drury 1983; Kang & Ryu 2011). In Figure 1, we show an example of $f_{e,\text{foss}}(p)$ with $s = 4.7$, and $p_c/m_e c = 10^3$ marked by the black dashed line, while its re-accelerated spectrum, $f_{e,\text{reacc}}(p)$, at a $M_s = 3$ shock is marked by the blue dot-dashed line. Note that the normalization factor is set to $f_o = f_{\text{ref}}$ in Equation (7) with $Q_{i,e} = 3.8$ for the purpose of illustration only.

For a power-law fossil population without a cutoff, $f_{e,\text{foss}} \propto p^{-s}$, the re-accelerated spectrum can be

obtained by direct integration (Kang & Ryu 2011): for $p \geq p_{\text{ref}}$

$$f_{e,\text{reacc}}(p) = \begin{cases} \frac{q}{(q-s)} [1 - (p/p_{\text{ref}})^{-q+s}] f_{e,\text{foss}}(p), & \text{if } q \neq s; \\ q \ln(p/p_{\text{ref}}) f_{e,\text{foss}}(p), & \text{if } q = s. \end{cases} \quad (13)$$

Although we do not explicitly show it here, the re-accelerated spectrum of pre-existing protons, $f_{p,\text{reacc}}(p)$, can be described by the same integration as Equation (12), except that the lower bound should be replaced with p_{inj} and $f_{e,\text{foss}}(p)$ should be replaced with a pre-existing proton population, $f_{p,\text{pre}}(p)$, with appropriate parameters, s , p_c , and f_o .

3. APPLICATION TO RADIO RELICS

3.1. DSA Model Spectrum

We use the DSA models given in Equations (6) and (12) to calculate the energy spectrum of accelerated electrons at weak shocks propagating into the preshock gas with $T_1 = 5.8 \times 10^7$ K. Panel (a) of Figure 2 shows the injection spectrum, $f_{e,\text{inj}}(p)$, for shocks with $M_s = 1.6 - 4.0$ (with increment $\Delta M_s = 0.2$). Considering that the synchrotron emission from mono-energetic electrons with the Lorentz factor, γ_e , peaks around the characteristic frequency, $\nu_{\text{peak}} \approx 130 \text{ MHz} (\gamma_e/10^4)^2 (B/1 \mu\text{G})$, we compare the amplitude of $f_{e,\text{inj}}(p_{\text{rad}})$, where $p_{\text{rad}} = 10^4 m_e c$, at the green vertical dashed line. The magenta line in Figure 3(a) illustrates how $f_{e,\text{inj}}(p_{\text{rad}})$ depends on the shock Mach number. In the case of the *in situ* acceleration model, $f_{e,\text{inj}}(p_{\text{rad}})$ increases by a factor of 4.2×10^3 for the range of $M_s = 2.0 - 3.0$. This strong dependence is even stronger at lower Mach number, so that $f_{e,\text{inj}}(p_{\text{rad}})$ decreases almost by a factor of 90, when M_s

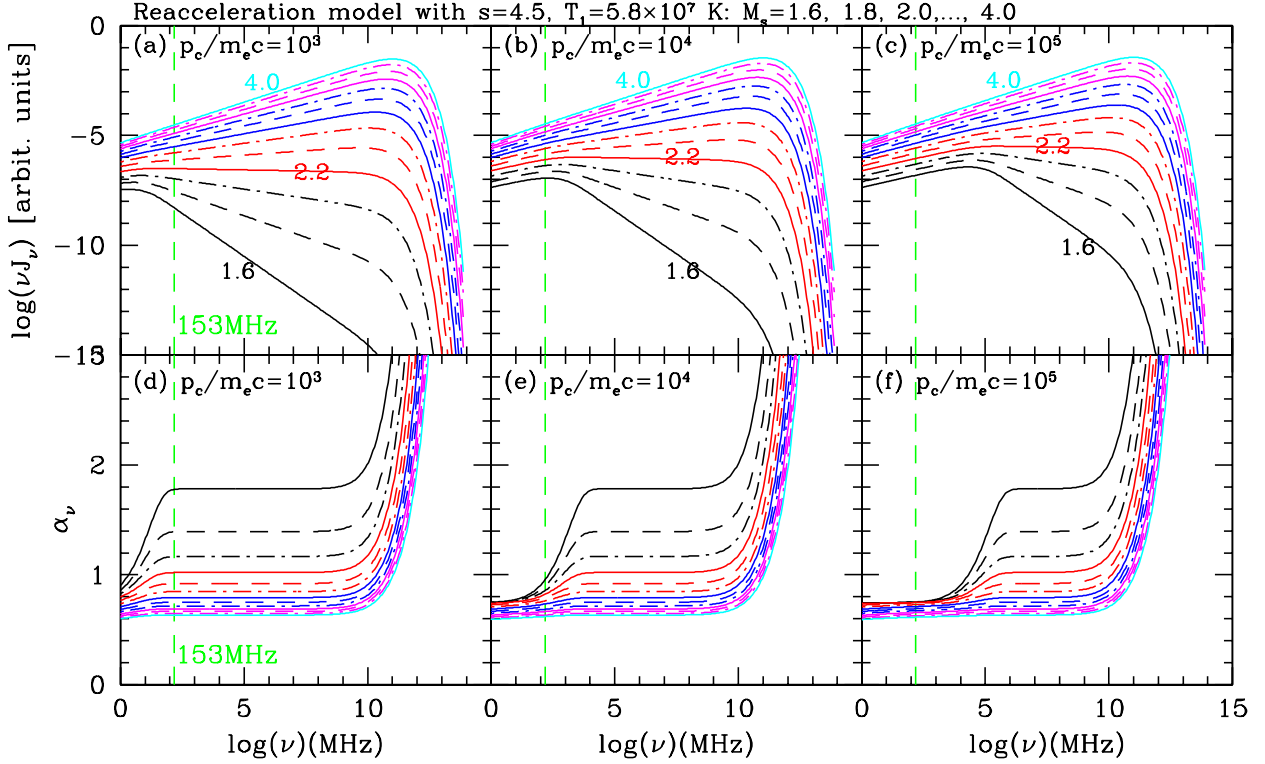


Figure 4. *Top panels:* Synchrotron spectrum, νj_ν , due to $f_{e,\text{reacc}}(p)$ re-accelerated at shock with $M_s = 1.6 - 4.0$ and $T_1 = 5.8 \times 10^7$ K in the presence of fossil CRe with the slope, $s = 4.5$, and the cutoff momentum, a) $p/m_e c = 10^3$, b) $p/m_e c = 10^4$, c) $p/m_e c = 10^5$. The semi-analytic DSA spectra ($Q_{i,e} = 3.8$) shown in Figure 2 are used. The emissivity νj_ν is plotted in arbitrary units. The blue dashed lines correspond to the models with $M_s = 3.0$ and $q = s = 4.5$. The green vertical lines denote $\nu = 153$ MHz. *Bottom panels:* Synchrotron spectral index, $\alpha_\nu = -d \ln j_\nu / d \ln \nu$, for the radiation spectra shown in the top panels. Note that the results for the *in situ* acceleration model are not shown because the corresponding synchrotron spectrum is a simple power-law with a cutoff.

decreases from 2.0 to 1.8. This implies that the radio surface brightness could vary extremely sensitively with M_s , when a radio relic consists of multiple shocks with slightly different Mach numbers (Roh et al. 2019).

Panels (b) and (c) of Figure 2 show the re-accelerated spectra, $f_{e,\text{reacc}}(p)$, of the fossil electron spectrum, $f_{e,\text{foss}}(p)$, with $s = 4.5$ and $p_c/m_e c = 10^3$ and 10^4 , respectively. Again, we set $f_o = f_{\text{ref}}$ with $Q_{i,e} = 3.8$ as in Figure 1. For stronger shocks with $M_s \geq 3.0$, the re-accelerated spectrum is flatter than the fossil spectrum, i.e., $q \leq s$. Hence fossil CRe serve only as seed particles, and so $f_{e,\text{reacc}}(p)$ does not depend on the cutoff momentum, p_c . For weaker shocks with $M_s < 3.0$, however, $q > s$. Hence, $f_{e,\text{reacc}}(p)$ depends on p_c for $p > p_c$, as can be seen in Figure 2. Thus, in the case of weaker shocks with $q > s$, the cutoff p_c should be high enough to obtain the simple power-law, $f_{e,\text{reacc}}(p) \propto p^{-s}$ for $p > p_{\text{rad}}$. Again, panel (a) of Figure 3 shows how $f_{e,\text{reacc}}(p_{\text{rad}})$ for the re-acceleration model depends on M_s for the three models of $p_c/m_e c = 10^3$ (black), 10^4 (red), and 10^5 (blue). It increases only by a factor of 55 for the range of $M_s = 2.0 - 3.0$ for the models with $p_c/m_e c = 10^3$. In the case of $p_c/m_e c = 10^5$, it increases by an even smaller factor, 9.6, for $M_s = 2.0 - 3.0$. Thus, the amplitude of $f_{e,\text{reacc}}(p_{\text{rad}})$ of radio-emitting elec-

trons for the re-acceleration model has a much weaker dependence on M_s , compared to $f_{e,\text{inj}}(p_{\text{rad}})$ for the *in situ* acceleration model. Moreover, this dependence becomes weaker if the cutoff momentum is higher than $p_c/m_e c \gtrsim 10^5$.

Panel (b) of Figure 3 shows the ratio $E_{\text{CRe}}/E_{\text{sh}}$ due to the following three CRe spectra: (1) $f_{e,\text{reacc}}(p)$ in the postshock region, (2) $f_{e,\text{foss}}(p)$ with $p_c/m_e c = 10^3$ in the preshock region, and (3) $f_{e,\text{inj}}(p)$ in the postshock region. With the adopted value of $Q_{i,e} = 3.8$, the *in situ* acceleration model (magenta asterisks) predicts that $E_{\text{CRe},2}/E_{\text{sh}} \approx 10^{-3.5} - 10^{-3}$ for $1.6 \lesssim M_s \lesssim 4.4$. In the case of the re-acceleration model with $s = 4.5$, $p_c/m_e c = 10^3$, and $f_o = f_{\text{ref}}$, the postshock ratio (closed circles) varies rather slowly, $E_{\text{CRe},2}/E_{\text{sh}} \approx 10^{-2.3} - 10^{-2.1}$. Of course, this ratio is arbitrary here and scales with the adopted normalization factor, f_o , of the fossil CRe population. Note that the preshock ratio (open circles), $E_{\text{CRe},1}/E_{\text{sh}}$, decreases with increasing M_s , because the denominator increases with M_s^2 .

3.2. Radio Synchrotron Emission

We now calculate the synchrotron volume emissivity, $j_\nu(\nu)$, due to $f_{e,\text{reacc}}(p)$ shown in Figure 2, with the postshock magnetic field strength, $B_2 = B_1 \sqrt{1/3 + 2\sigma^2/3}$

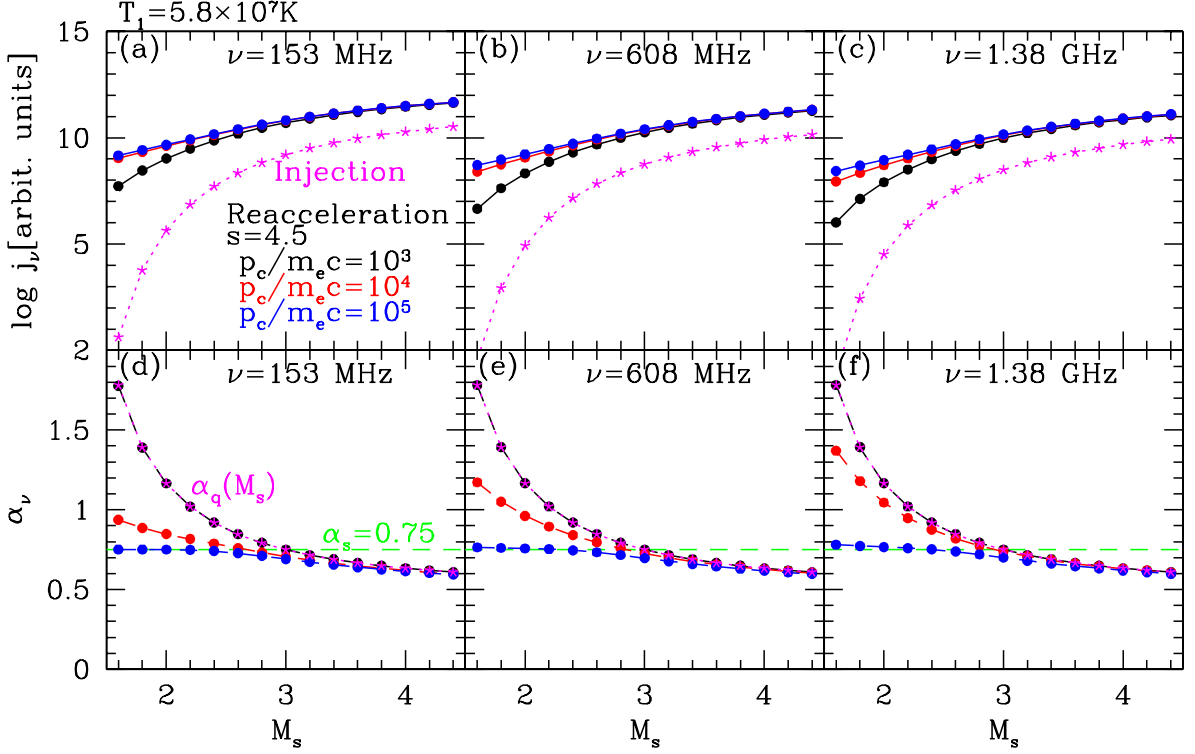


Figure 5. *Top panels:* Amplitudes of j_ν at 153 MHz, 608 MHz, and 1.38 GHz for the synchrotron spectra shown in Figure 4. Three models with fossil CRE with slope $s = 4.5$, and cutoff momentum $p/m_e c = 10^3$ (black circles), 10^4 (red circles), and 10^5 (blue circles) are shown. The magenta lines with asterisks show the same quantities for the injection-only case. Note that j_ν scales with the adopted normalization factor, f_o and is plotted in arbitrary units here. *Bottom panels:* Synchrotron spectral index, $\alpha_\nu = -d \ln j_\nu / d \ln \nu$, for the same models shown in the upper panels. Note that the black line (re-acceleration case with $p/m_e c = 10^3$) coincides with the magenta line (injection-only case), which also corresponds to $\alpha_q(M_s) = (q - 3)/2$. The green horizontal lines denote $\alpha_s = (s - 3)/2 = 0.75$.

(where $B_1 = \mu G$), in order to illustrate how the radio spectrum changes with the shock Mach number. We do not show explicitly the emissivity spectrum for the *in situ* acceleration case, since both $f_{e,\text{inj}}(p)$ and $j_\nu(\nu)$ are simple power-laws with an exponential cutoff.

The top panels of Figure 4 shows νj_ν , while the bottom panel shows its spectral index, $\alpha_\nu = -d \ln j_\nu / d \ln \nu$. Note that j_ν scales with the adopted normalization factor, f_o and is plotted in arbitrary units here. For stronger shocks with $q < s$, $j_\nu(\nu)$ is a power-law with $\alpha_q = (q - 3)/2 = (M_s^2 + 3)/2(M_s^2 - 1)$ with a cutoff. For weaker shocks with $q > s$, however, the radio spectrum depends on the cutoff momentum of the fossil CRE spectrum, p_c , as well as M_s , as expected from $f_{e,\text{reacc}}(p)$ in Figure 2. At these weaker shocks, the slope, α_ν , gradually increases from $(s - 3)/2$ to $(q - 3)/2$, as the frequency increases. Hence, the fossil CRE power-law should extend to well above $p_c/m_e c \gtrsim 10^5$, in order for the spectral index to be determined by the slope of fossil CRE, i.e., $\alpha_s = (s - 3)/2$, for $\nu \lesssim 10$ GHz (see panel (f) of Figure 4). For example, if the power-law spectrum of fossil CRE extends only up to $p_c/m_e c \lesssim 10^3$, the radio spectral index due to postshock CRE becomes $(q - 3)/2$ for $\nu \gtrsim 153$ MHz (see panel (d) of Figure 4).

Figure 5 shows the relative values of j_ν and α_ν at

three typical observation frequencies, $\nu_{\text{obs}} = 153$ MHz, 608 MHz, and 1.38 GHz (e.g., van Weeren et al. 2010). Similarly to the case of $f(p_{\text{rad}})$, both $j_\nu(\nu_{\text{obs}})$ and $\alpha_\nu(\nu_{\text{obs}})$ vary strongly with M_s for the *in situ* acceleration model (magenta asterisks). For example, $j_{153\text{MHz}}$ increases by a factor of 3.7×10^3 , $j_{608\text{MHz}}$ by a factor of 6.5×10^3 , and $j_{1.38\text{GHz}}$ by a factor of 9.2×10^3 , as M_s increases from 2.0 to 3.0; the Mach number dependence is a bit stronger at higher observational frequencies. Again, the re-acceleration models (filled circles) exhibit much weaker dependence on M_s . For the model with $p_c/m_e c = 10^3$ (black filled circles), $j_{153\text{MHz}}$ increases by a factor of 48, and $j_{1.38\text{GHz}}$ by a factor of 120 for $M_s = 2.0 - 3.0$. For the model with $p_c/m_e c = 10^5$ (blue filled circles), $j_{153\text{MHz}}$ increases only by a factor of 14, and $j_{1.38\text{GHz}}$ by a factor of 16 for $M_s = 2.0 - 3.0$.

For stronger shocks with $q \leq s$, even the re-acceleration models have a spectral index that follows the injection index, α_q (magenta asterisks); thus, in the bottom panels of Figure 5, all symbols (black, red, blue, and magenta) overlap for $M_s \geq 3.0$. For weaker models with $q > s$, the spectral index depends again on p_c . For the models with $p_c/m_e c = 10^5$ (blue filled circles), $\alpha_\nu \approx \alpha_s$ for $M_s < 3$. In the case of the models $p_c/m_e c = 10^3$ (black filled circles), the fossil CRE serve

as only seed particles, so the spectral indices at the three observational frequencies become the same as the injection index, $\alpha_q(M_s)$.

In conclusion, if a radio relic is composed of multiple shocks with slightly different Mach numbers (Roh et al. 2019), the surface brightness fluctuations could be much larger in the *in situ* acceleration model, compared to the re-acceleration model. The variations in the spectral index profile should be much smaller, however. Relatively smooth profiles of radio flux along the edge of some observed radio relics, such as the Sausage relic (Hoang et al. 2017) and the Toothbrush relic (van Weeren et al. 2016), probably indicate that re-acceleration plays a significant role there.

4. SUMMARY

Based on recent studies using plasma kinetic simulations (e.g., Guo et al. 2014; Matsukiyo & Matsumoto 2015; Park et al. 2015; Kang et al. 2019; Trotta & Burgess 2019; Kobzar et al. 2019), we suggest semi-analytic DSA models for the electron (re-)acceleration at weak Q_\perp -shocks in the test-particle regime. They rely on the following working assumptions: (1) at Q_\perp -shocks of all Mach numbers in the test-particle regime (i.e., $M_s \lesssim 4$), electrons can be pre-accelerated from the thermal pool by both electron and ion kinetic instabilities and injected to the DSA process, and (2) the momentum distribution function of (re-)accelerated electrons follows the prediction of the DSA theory for $p \geq p_{\text{ref}} = Q_{i,e} p_{\text{th},e}$ with $Q_{i,e} \approx 3.5 - 3.8$. However, it remains uncertain if and how subcritical shocks with $M_s \lesssim 2.3$ could inject electrons to the DSA process (Kang et al. 2019) or re-accelerate pre-existing fossil CR electrons through DSA. We include the electron (re-)acceleration in subcritical shocks here, because in some of observed radio relics the shock Mach number is estimated to be less than 2.3 (e.g., van Weeren et al. 2016).

Then, the momentum distribution of accelerated electrons can be represented by the simple power-law with a cutoff given in Equation (6) for the *in situ* acceleration model. For the re-acceleration model with fossil CRe, which is specified by three parameters, the slope, s , the cutoff, p_c , and the normalization factor, f_o , the re-accelerated spectrum can be integrated semi-analytically as in Equation (12).

We explore how our model spectrum of CRe varies with the parameters such as M_s , s , and p_c in the case of weak shocks with $M_s = 1.6 - 4.4$ for the two types of DSA models: the *in situ* acceleration model and the re-acceleration model. The main findings can be summarized as follows:

1. For stronger shocks with $q = 4M_s^2/(M_s^2 - 1) \leq s$, the re-accelerated spectrum becomes a power-law, $f_{e,\text{reacc}}(p) \propto p^{-q}$, and does not depend on p_c . The radio synchrotron spectrum likewise becomes a power-law with $\alpha_\nu \approx \alpha_q = (q - 3)/2 = (M_s^2 + 3)/(2(M_s^2 - 1))$ and an appropriate cutoff.
2. For weaker shocks with $q > s$, on the other hand, $f_{e,\text{reacc}}(p)$ depends on the cutoff p_c . Only for

$p_c/m_e c \gtrsim 10^5$, the radio synchrotron spectrum has a spectral index, $\alpha_\nu \approx \alpha_s = (s - 3)/2$ for observation frequencies in the range $\nu_{\text{obs}} \approx 100 \text{ MHz} - 10 \text{ GHz}$.

3. If $p_c/m_e c \lesssim 10^3$, the fossil CRe provide only seed particles to DSA, and hence the spectral index is similar to the injection index, $\alpha_\nu \approx \alpha_q$.
4. In the *in situ* acceleration model, the radio synchrotron emissivity, j_ν , depends strongly on M_s , and it increases by a factor of $10^3 - 10^4$ as M_s increases from 2.0 to 3.0. But it varies by a factor of only about 15 in the re-acceleration model with $p_c/m_e c = 10^5$ for the same range of M_s . In the case of a lower cutoff at $p_c/m_e c = 10^3$, $j_{153\text{MHz}}$ increases by a factor of 48, and $j_{1.38\text{GHz}}$ by a factor of 120 for the same range of M_s .

Considering that the spatial profiles of radio flux and spectral index vary rather smoothly along the edge of some observed radio relics (e.g., van Weeren et al. 2016; Hoang et al. 2017), and that giant radio relics on Mpc scales are likely to consist of multiple shocks with different M_s (e.g., Roh et al. 2019), our results imply that the re-acceleration of fossil CRe is important in understanding the origin of radio relics.

ACKNOWLEDGMENTS

This work was supported by a 2-Year Research Grant of Pusan National University. The author thanks D. Ryu for stimulating discussions at the initial stage of this work.

REFERENCES

- Akamatsu, H. & Kawahara, H. 2013, Systematic X-Ray Analysis of Radio Relic Clusters with Suzaku, PASJ, 65, 16
- Amano, T. & Hoshino, M. 2009, Electron Shock Surfing Acceleration in Multidimensions: Two-Dimensional Particle-in-Cell Simulation of Collisionless Perpendicular Shock, ApJ, 690, 244
- Balogh, A. & Truemann, R. A., 2013, Physics of Collisionless Shocks: Space Plasma Shock Waves, ISSI Scientific Report 12 (New York: Springer)
- Bell, A. R. 1978, The Acceleration of Cosmic Rays in Shock Fronts – I, MNRAS, 182, 147
- Brunetti, G., & Jones, T. W. 2014, Cosmic Rays in Galaxy Clusters and Their Nonthermal Emission, Int. J. Mod. Phys. D, 23, 30007
- Burgess, D. 2007, Particle Acceleration at the Earth's Bow Shock, Lect. Notes Phys., 725, 161
- Caprioli, D., & Spitkovsky, A. 2014, Simulations of Ion Acceleration at Non-relativistic Shocks. I. Acceleration Efficiency, ApJ, 783, 91
- Caprioli, D., Pop, A. R., & Spitkovsky, A. 2015, Simulations and Theory of Ion Injection at Non-relativistic Collisionless Shocks, ApJ, 798, 28
- Drury, L. O'C. 1983, An Introduction to the Theory of Diffusive Shock Acceleration of Energetic Particles in Tenuous Plasmas, Rep. Prog. Phys., 46, 973
- Feretti, L., Giovannini, G., Govoni, F., & Murgia, M. 2012, Clusters of Galaxies: Observational Properties of the Diffuse Radio Emission, A&A Rev., 20, 54

- Gosling, J. T., Thomsen, M. F., & Bame, S. J. 1989, Suprathermal electrons at Earth's bow shock, *JGR*, 94, 10011
- Guo, X., Sironi, L., & Narayan, R. 2014, Non-thermal Electron Acceleration in Low Mach Number Collisionless Shocks. I. Particle Energy Spectra and Acceleration Mechanism, *ApJ*, 793, 153
- Ha, J.-H., Ryu, D., Kang, H., & van Marle, A. J. 2018, Proton Acceleration in Weak Quasi-parallel Intracluster Shocks: Injection and Early Acceleration, *ApJ*, 864, 105
- Hoang, D. N., Shimwell, T. W., Stroe, A. et al. 2017, Deep LOFAR Observations of the Merging Galaxy Cluster CIZA J2242.8+5301, *MNRAS*, 471, 1107
- Kang, H. 2011, Energy Spectrum of Nonthermal Electrons Accelerated at a Plane Shock, *JKAS*, 44, 49
- Kang, H. 2016, Re-acceleration Model for the Toothbrush Radio Relic, *JKAS*, 49, 83
- Kang, H., Jones, T. W., & Gieseler, U. D. J. 2002, Numerical Studies of Cosmic-Ray Injection and Acceleration, *ApJ*, 579, 337
- Kang, H. & Ryu, D. 2011, Re-acceleration of Non-thermal Particles at Weak Cosmological Shock Waves, *ApJ*, 734, 18
- Kang, H., Ryu, D., & Jones, T. W. 2012, Diffusive Shock Acceleration Simulations of Radio Relics, *ApJ*, 756, 97
- Kang, H., Ryu, D., & Jones, T. W. 2017, Shock Acceleration Model for the Toothbrush Radio Relic, *ApJ*, 840, 42
- Kang, H., Ryu, D., & Ha, J.-H. 2019, Electron Pre-acceleration in Weak Quasi-perpendicular Shocks in High-beta Intracluster Medium *ApJ*, 876, 79
- Levinson, A., 1992, Electron Injection in Collisionless Shocks, *ApJ*, 401, 73
- Levinson, A., 1996, On the Injection of Electrons in Oblique Shocks, *MNRAS*, 278, 1018
- Malkov, M. A. & Drury, L.O'C. 2001, Nonlinear Theory of Diffusive Acceleration of Particles by Shock Waves, *Rep. Progr. Phys.*, 64, 429
- Marcowith, A., Bret, A., Bykov, A., et al. 2016, The Microphysics of Collisionless Shock Waves, *RPPH*, 79, 046901
- Matsukiyo, S. & Matsumoto, Y. 2015, Electron Acceleration at a High Beta and Low Mach Number Rippled Shock *J. Phys. Conf. Ser.*, 642, 012017
- Kobzar, O., Niemiec, J., Amano, T., et al. 2019, Electron Acceleration at Rippled Low Mach Number Shocks in Merging Galaxy Clusters, *Proc. 36th Int. Cosmic Ray Conf. (ICRC2019)*, 368
- Park, J., Caprioli, D., & Spitkovsky, A. 2015, Simultaneous Acceleration of Protons and Electrons at Nonrelativistic Quasiparallel Collisionless Shocks, *PRL*, 114, 085003
- Riquelme, M. A. & Spitkovsky, A. 2011, Electron Injection by Whistler Waves in Non-relativistic Shocks, *ApJ*, 733, 63
- Roh, S., Ryu, D., Kang, H., Ha, S., & Jang, H. 2019, Turbulence Dynamo in the Stratified Medium of Galaxy Clusters, *ApJ*, 883, 138
- Ryu, D., Kang, H., Hallman, E., & Jones, T. W. 2003, Cosmological Shock Waves and Their Role in the Large-Scale Structure of the Universe, *ApJ*, 593, 599
- Ryu, D., Kang, H., & Ha, J.-H. 2019, A Diffusive Shock Acceleration Model for Protons in Weak Quasi-parallel Intracluster Shocks *ApJ*, 883, 60
- Trotta, D. & Burgess, D. 2019, Electron Acceleration at Quasi-perpendicular Shocks in Sub- and Supercritical Regimes: 2D and 3D Simulations, *MNRAS*, 482, 1154
- van Weeren, R., Röttgering, H. J. A., Brügger, M., & Hoeft, M. 2010, Particle Acceleration on Megaparsec Scales in a Merging Galaxy Cluster, *Science*, 330, 347
- van Weeren, R. J., Brunetti, G., Brügger, M., et al. 2016, LOFAR, VLA, and CHANDRA Observations of the Toothbrush Galaxy Cluster, *ApJ*, 818, 204
- van Weeren, R. J., de Gasperin, F., Akamatsu, H., et al. 2019, Diffuse Radio Emission from Galaxy Clusters, *Space Sci. Rev.*, 215, 16
- Vazza, F., Brunetti, G., & Gheller, C. 2009, Shock Waves in Eulerian Cosmological Simulations: Main Properties and Acceleration of Cosmic Rays, *MNRAS*, 395, 1333
- Wittor, D. Vazza, F. & Brügger, M. 2017, Testing Cosmic Ray Acceleration with Radio Relics: a High-resolution Study Using MHD and Tracers, *MNRAS*, 464, 4448